Article

Enhancement of Thermoelectric Performance for InTe by Selective Substitution and Grain Size Modulation

Menghui Zhou [1,2], Juan Li [2], Guoying Dong [1,2], Shufang Gao [1,*], Jianghe Feng [2,*] and Ruiheng Liu [2]

1 School of Physics and Optoelectronic Engineering, Yangtze University, Jingzhou 434023, China
2 Shenzhen Institute of Advanced Electronic Materials, Shenzhen Institute of Advanced Technology, Chinese Academy of Sciences, Shenzhen 518055, China
* Correspondence: 501147@yangtzeu.edu.cn (S.G.); jh.feng@siat.ac.cn (J.F.)

Abstract: The different masses, ionic radii, and chemical valences of the nonequivalent crystallographic sites of thermoelectric (TE) compounds provide an effective way to modulate the thermoelectric performance by selective substitution. In this work, the selective substitution of In^+ by Pb for the binary InTe material monotonically reduces the carrier concentration, which is greatly beneficial to the mechanism investigation of serious grain boundary scattering (GBS). This is the first time this point has been mentioned with regard to InTe material. As a result, we found that GBS was dominated by the grain size when the carrier concentration was higher than 0.7×10^{19} cm^{-3} but was inversely governed by the carrier concentration when the carrier was situated at a lower density. In particular, the occupation of Pb on the targeted In^+ site could further reduce the lattice thermal conductivity. Finally, $In_{0.9999}Pb_{0.0001}Te$ achieved the improved power factor and average zT value, which could contribute to high-power generation below a medium temperature. This effect of increasing the carrier concentration on the suppression of GBS sheds light on the possibility of improving electron mobility by increasing the carrier concentration.

Keywords: InTe; thermoelectric performance; grain size; carrier concentration; grain boundary scattering

1. Introduction

Thermoelectric (TE) materials have the ability to create direct conversion between heat and electricity without any moving parts or noise; they are regarded as eco-friendly energy materials and have attracted intensive attention in the scientific community [1–3]. The heat-to-power conversion efficiency (η) is strongly related to the materials' dimensionless figure of merit, $zT = S^2\sigma T/(\kappa_L + \kappa_e)$, where T, σ, S, κ_L, and κ_e are the absolute temperature, electrical conductivity, Seebeck coefficient, lattice, and electron thermal conductivity [4]. The strong coupling of S, σ, and κ_e through carrier concentration makes it extremely difficult to improve the zT value. Thus, it requires the band engineering of degeneracy [5,6], curvature [7], and valley anisotropy to improve the electronic performance as well as microstructural defect engineering to reduce the independent κ_L in order to increase the thermoelectric performance [8–11]. In addition, the exploration of new materials with low κ_L provides an effective way to achieve outstanding TE properties [9,10,12–17].

The new rising binary InTe possesses a typical characteristic of phonon-glass electron-crystal (PGEC) [18,19]. It features a TlSe-type structure with one directional (1D) strong covalent chains of $[In^{3+}Te_{4/2}^{2-}]^-$ along a c direction, which are further weakly bridged by an In^+ cation with $5s^2$ lone pair electrons [20]. The weak ionic bonds result in the large anharmonic vibrations of In^+ and the strong anharmonic phono–phonon interactions, which induce an extremely low κ_L even for the single crystal of InTe. In recent years, the high TE performance has been obtained by atomic doping and single crystal growth [16,21–27], which promotes the peak zT high up to 1.2 @648 K [15]. Compared with the varied doping results of Cu, Na [27], Cd [23], Sb [22], Pb [21], Ga [15], etc., Pb:InTe achieved the lowest

lattice thermal conductivity, which was derived from the anharmonic vibrations of In$^+$ and the selective doping at the In$^+$ site for the different ionic radii ($r_{In^+} > r_{Pb^{2+}} > r_{In^{3+}}$).

On the other hand, lattice thermal conductivity is totally governed by specific heat C_V, phonon group velocity v, and the mean free path of the heat-carrying phonon, i.e., $\kappa_L = C_V v l$. The inherently anharmonic vibrations have generated a low v and κ_L for InTe. In addition, the l can also be modulated to further reduce the κ_L since it mainly depends on the phonon scattering mechanism, such as phonon–phonon scattering, microstructural defect scattering, and nanoparticle scattering. However, the previous investigation of polycrystalline InTe with varied grain sizes indicated that the reduction in grains actually reduced κ_L but also caused it to be strongly scattered by the grain boundary (GB) of the carrier, which resulted in low electrical conductivity below ~500 K [15,21,22] and severely deteriorated the TE performance at room temperature. Therefore, how to enhance the phonon scattering but not seriously affect the carriers' transportation becomes the main purpose for grain size modulation. In principle, GBS is related to the Fermi level, grain size, grain boundary barrier, and so on for materials [15,22], resulting in the strong relationship of the GBS and the carrier concentration. Up to now, how the carrier concentration affects the GBS is rarely mentioned for InTe. Thus, it prompted us to explore the synergistic effect of grain size and carrier concentration on depressing GBS based on varied grain sizes with a monotonic reduction in the carrier concentration.

In this work, we systematically investigated the effects of Pb doping amounts and grain sizes on the modulation of the electron and phonon transports of InTe. In addition, the Pb doping could monotonically reduce the carrier concentration, which provided the opportunity to explore the effect of carrier concentration on the suppression of GBS for InTe. As a result, both grain size and carrier concentration significantly influenced the GBS. The GBS could be depressed by increasing the grain size only when the carrier concentration was larger than 0.7×10^{19} cm^{-3}. In addition, Pb doping also greatly reduced the lattice thermal conductivity. Therefore, the improved zT value below 600 K for Pb$_{0.0001}$In$_{0.9999}$Te was obtained, which was beneficial to the power generation below medium temperature. Furthermore, this effect of carrier concentration on the suppression of GBS illustrated the possibility of electron mobility improvement by increasing the carrier concentration.

2. Materials and Methods

In order to synthesize the pure phase of In$_{1-x}$Pb$_x$Te (x = 0, 0.0001, 0.001, 0.003, 0.005), the high-purity (>99.99%) indium, lead, and tellurium particles were weighed in stoichiometric ratios and then loaded into the carbon-coated quartz tubes. The indium, lead, and tellurium particles were produced by Zhongnuo Advanced Material Technology Co., Ltd (Beijing, China). Additionally, due to the very small doping amount of Pb, the total amount in our experiment was >20 g. However, in this situation, for Pb$_{0.0001}$In$_{0.9999}$Te the amount of Pb was >2 mg, which could be accurately weighed because the weighing error was only ±0.0005 g. Subsequently, the quartz tubes were sealed with a vacuum of ~10^{-1} Pa. The tubes containing In, Te, and Pb were heated to 1123 K in 7 h and then held at this temperature for 4 h before the furnaces were switched off. The obtained InTe ingot was hand-ground and sieved with two particle size ranges of >150 μm (80 mesh) and <50 μm (300 mesh), respectively (marked as InTe-Coarse and InTe-Fine, respectively), and the other ingots of In$_{1-x}$Pb$_x$Te (x = 0.0001, 0.001, 0.003, 0.005) were hand-ground and sieved with only large sizes of >150 μm. Finally, these powders were loaded into graphite dies with an inner diameter of 10 μm, which were placed in the hot-press sintering furnace (NYRH-HP). The sintering was operated under a uniaxial pressure of 50 MPa with a vacuum <5 Pa at 773 K for 30 min, producing pellets with high densities (>95% of the theoretical densities), which were then cut into small samples with dimensions of 10 × 2 × 2 mm^3 and 6 × 6 × 1.5 mm^3 for measurements of the electrical and thermal properties. It needs to be mentioned that the electrical and the thermal conductivity were measured along the pressure direction due to the anisotropic atomic structure of InTe and the high texture degree of the (110) along this direction.

The phase purity of the samples was confirmed by powder X-ray diffraction (PXRD) using a Bruker AXSD8 Adance X diffractometer (Saarbrücken, Germany) with Cu K_α radiation of 1.5406 Å at room temperature. A scanning electron microscope (Thermo Scientific Apreo 2 S HiVac, 5 kV, Waltham, America) equipped with an energy-dispersive X-ray spectrometer (EDS, Waltham, America) was used to investigate the microstructures and chemical compositions. The electrical conductivity and Seebeck coefficient were measured using an Ulvac ZEM-3 (Chigasaki, Japan) from 300 K to 773 K, based on the same sample. The thermal diffusivity (D) was measured between 300 K and 773 K by using the laser flash diffusivity technique on an LFA-467 instrument (Netzsch, Selb, Germany). The total thermal conductivity was calculated using the relation of $\kappa = DC_p\rho$, where ρ is the density of the sample measured by the Archimedes method, and C_p is the specific heat capacity using the Dulong–Petit estimation, due to the low Debye temperature of around 200 K [22]. The Hall coefficients (R_H) were measured by the van der Pauw technique with a Xiangjin self-made Hall electrical performance test system (NYMS) under a helium atmosphere. The Hall carrier concentrations (n_H) and Hall mobilities (μ_H) were estimated by $n_H = 1/eR_H$ and $m_H = sR_H$, respectively.

3. Results and Discussion

The obtained samples of $In_{1-x}Pb_xTe$ (x = 0, 0.0001, 0.001, 0.003, 0.005) showed high phase purity, which could be verified by the good agreement of their PXRD pattern positions with the standard JCPDS card (PDF#81-1972) of the InTe, as shown in Figure 1a. However, the different intensities of the PXRD peaks for the samples revealed their varied texture degrees. In detail, through the grain size modulation, the texture degree of the ($ll0$) plane could be increased from 0.01 to > 0.1, which was calculated by the formula:

$$F = \frac{P - P_0}{1 - P_0}, \ P_0 = \frac{I_0(00l)}{\Sigma I_0(hkl)}, \ P = \frac{I(00l)}{\Sigma I(hkl)} \tag{1}$$

where $I(hkl)$ and $I_0(hkl)$ are the peak integral intensities for the measured and randomly oriented samples, respectively [28]. In addition, the Pb-doped samples with large grain sizes also had the large orientation factor $F(ll0)$, which was similar to that of the coarse pure polycrystalline InTe. This improved texture degree was highly beneficial to the utilization of the expected anisotropic transports of higher electrical conductivity and lower thermal conductivity along the [110] direction; this was confirmed by the investigation of the transports based on a single InTe crystal and could be taken advantage of to improve the TE performance of InTe [29]. Furthermore, the cell parameters were refined based on the XRD data, and the results are shown Figure 1b. It can be seen that the lattice gradually decreases with the increase in the Pb doping concentration, which is consistent with our experimental design with regard to the substitution of In+ by Pb^{2+} ions, because of their different ionic radii $r_{In^+} > r_{Pb^{2+}} > r_{In^{3+}}$. In addition, the pure phases can also be confirmed by the uniform distribution of the elements, which can be seen from the EDS results presented in Figure 1c because there is no second phase that can be observed.

The SEM results are displayed in Figure 2, which clearly shows that the average grain sizes of the sieved coarse $In_{1-x}Pb_xTe$ (x = 0, 0.0001, 0.001, 0.003, 0.005) are larger than 150 μm, and this value is much larger than that of InTe-Fine (<50 μm). According to the previous studies, the large grain sizes are beneficial to the depression of the GBS of InTe and can be expected to considerably improve the carrier mobility below 500 K [15,30,31]. Therefore, the samples with large grains can remove the influence of the grain size when analyzing the relation of the carrier concentration and the GBS in this work.
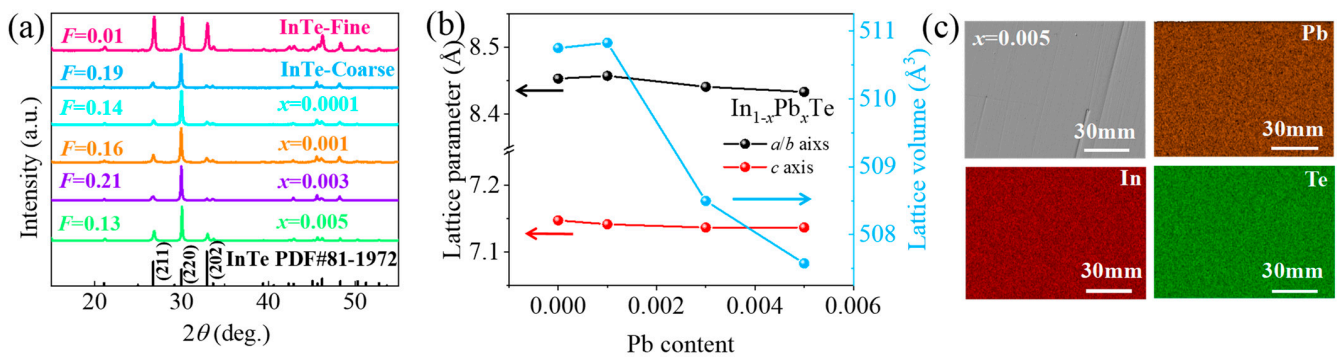
Figure 1. (**a**) The PXRD patterns of samples for the sieved coarse $In_{1-x}Pb_xTe$ (x = 0, 0.0001, 0.001, 0.003, 0.005) and the sieved fine InTe. (**b**) The lattice parameter dependence on the Pb dopant concentration. (**c**) SEM image and corresponding EDS compositional mappings for the sieved coarse $In_{0.995}Pb_{0.005}Te$ sample.
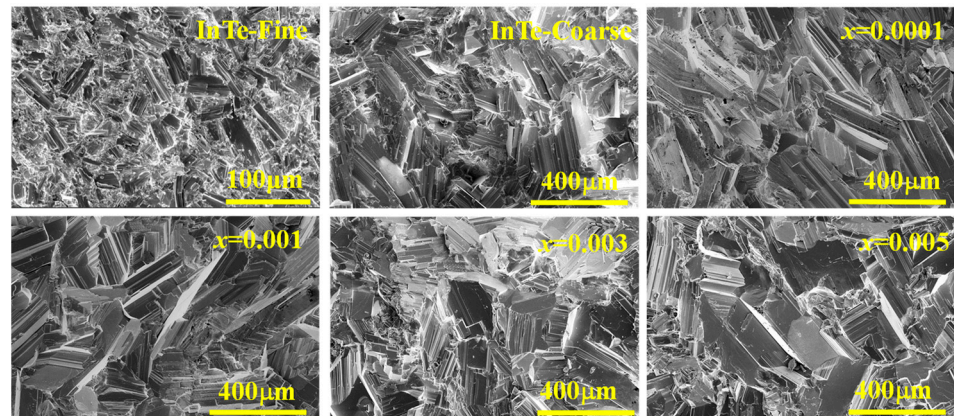

Figure 2. Cross-section SEM images for the sieved fine InTe and coarse $In_{1-x}Pb_xTe$ (x = 0, 0.0001, 0.001, 0.003, 0.005).

Figure 3 displays the electrical performance of the $In_{1-x}Pb_xTe$ (x = 0, 0.0001, 0.001, 0.003, 0.005) samples. As shown in Figure 3b, the σ reduces with the rising Pb doping ratio. In terms of the crystal structure, the In atom has two independent crystallographic sites of In^+ and In^{3+}, and the In^+ cation with $5s^2$ lone pair electrons has a larger size than the In^{3+} cation. Considering the large difference in the ionic radii of In^+ (1.32 Å), In^{3+} (0.81 Å), and Pb^{2+} (1.19 Å) [32,33], Pb^{2+} prefers to replace In^+ to locate between the covalent chains, which can reduce the carrier concentrations, as displayed in Figure 3a,c, and can give rise to the reduction in the σ with the increase in the doping amount, as shown in Figure 3b. This result is consistent with the reduced cell parameters resulting from the increasing of the doping ratio.

It should be noted that the temperature-dependent conductivity shows greatly different trends for $In_{1-x}Pb_xTe$ (x = 0, 0.0001, 0.001, 0.003, 0.005) with the varied carrier concentration. As shown in Figure 3b, the temperature-dependent electrical conductivity of coarse InTe presents a monotonically decreased trend which is similar to that of the single crystal due to the depression of GBS [29]. Although they have the smaller n, the σ of coarse InTe and $Pb_{0.0001}In_{0.9999}Te$ at room temperature are definitely much higher than those of the samples with fine grains [21]. These results are consistent with those in the literature on depressing GBS by increasing the grain size. However, when the carrier concentration is reduced, the electrical conductivity trend changes from a monotonic decrease to one which first rises then falls, even with samples with coarse grains. This situation has not been observed in other works of InTe. In order to analyze the mechanism of carrier scattering in detail, the carrier mobility was calculated based on the temperature-dependent carrier concentration, as shown in Figure 3d. When the doping ratio is lower than 0.1%, the μ_H

shows the temperature-dependent behaviors of $T^{-1.04}$ for $x = 0.0001$ and $T^{-0.89}$ for $x = 0.001$ within 300–423 K (Figure 3d), which is close to the acoustic phonon scattering (APS) relation of $T^{-1.5}$. However, the μ_H shows a $T^{-0.52}$ relation when the doping ratio is higher than 0.3% and the n_H is smaller than 0.7×10^{19} cm^{-3}, indicating the strengthened GBS and weakened APS when the carrier concentration is reduced.
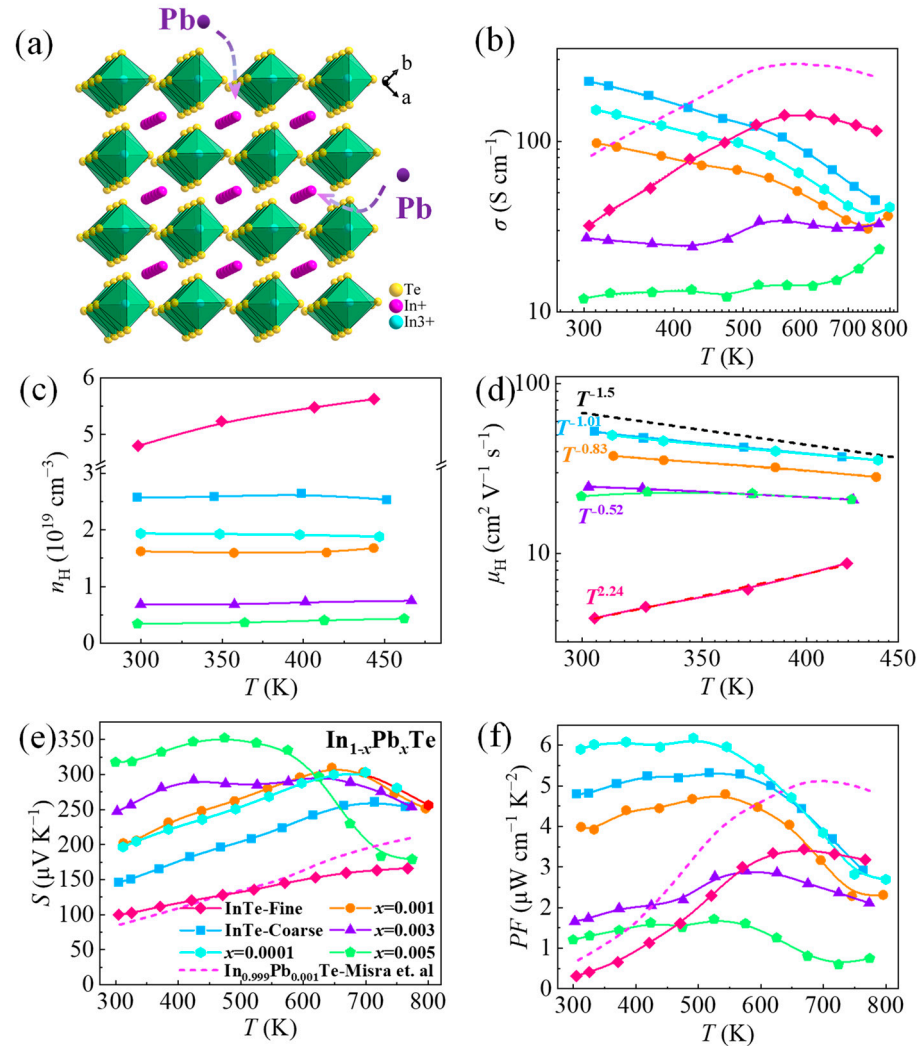
Figure 3. (**a**) Diagram of the Pb doping at In$^+$ site in InTe with the covalent chained crystal structure. Temperature dependence of the electrical properties of the sieved fine InTe and coarse In$_{1-x}$Pb$_x$Te (x = 0, 0.0001, 0.001, 0.003, 0.005). (**b**) Electrical conductivity, (**c**) Hall carrier concentration, (**d**) Hall carrier mobility, (**e**) Seebeck coefficient, and (**f**) power factor [21].

Academically, the GBS is related to the potential barrier (E_b) of the GB based on the trapping state model [34–36], which is expressed as:

$$E_b = \begin{cases} \frac{e^2 d^2 N}{8\varepsilon} & dN < Q_t \\ \frac{e^2 Q_t}{8N\varepsilon} & dN > Q_t \end{cases} \tag{2}$$

where d is the grain size, e is the elementary charge (C), ε is the dielectric constant, Q_t is the density of the trapping states at the grain boundaries (C m^{-2}), and N is originally defined as the concentration of ionized impurity atoms for the intrinsic semiconductor (usually dopant atoms, m^{-3}), which reflects the carrier concentration. Therefore, the E_b of the TE material largely depends on the carrier concentration and the grain size. Generally, there are three different situations in which to estimate the E_b: (1) when the carrier concentration is high

enough, the E_b could be very weak and can be ignored regardless of whether the grain size is large or small, which has been verified in other materials with high carrier concentration; (2) for TE materials with a normal carrier concentration, merely growing the grain size can reduce the Q_t and then depress the E_b and GBS, which is commonly used to remove the GBS of TE materials [31,37,38]; and (3) when the grain size is large enough, reducing the carrier concentration can still elevate the E_b and then promote the GBS, which is merely mentioned in electrical transport [30,39]. In this work, even for the coarse polycrystalline InTe, when raising the Pb doping ratio higher than 0.3%, the decreased n_H contributes to the increase in E_b and magnifies the GBS effect. The increase in carrier concentration to suppress the GBS illustrates the possibility of improving electron mobility by increasing the carrier concentration.

The positive Seebeck coefficients of all the samples reveal their p-type transports, as displayed in Figure 3e. With the doping ratio increasing, the room temperature S monotonically enhances due to the reduction in carrier concentration. It is interesting that the Seebeck coefficients are approached even with the different doping ratios at high temperature; this originates from the different intensity of the bipolar transports resulting from the thermal activation of the samples. This can also be reflected in their different band gaps (E_g) because the E_g of the samples decrease from 0.42 eV to 0.33 eV with the increase in the Pb doping amount, according to the calculation based on the Seebeck coefficient in the following formula [40]:

$$E_g = 2eS_{max}T_{(Smax)} \tag{3}$$

where S_{max} and $T_{(Smax)}$ are the peak Seebeck coefficient and the corresponding temperature, respectively. Specifically, the reduced E_g lowers the thermal activation temperature of the electron, and these thermally excited electrons reduce the S significantly at the high temperature due to the involvement of two kinds of carrier, which is expressed as [40]:

$$S = \frac{S_n\sigma_n + S_p\sigma_p}{\sigma_n + \sigma_p} \tag{4}$$

where S_n, S_p, s_n, and s_p are the Seebeck coefficient and the electrical conductivity for the electron (n) or hole (p), respectively. Therefore, a suitable band gap is important for the thermoelectric material to achieve high a Seebeck coefficient. Finally, the improved S of $In_{0.9999}Pb_{0.0001}Te$ and the high σ give rise to the 20% increment of the power factor (*PF*) near room temperature, as shown in Figure 3f. However, with the increasing doping amount of Pb, the *PF* will monotonically reduce because of the reduction in σ, which originates from the low carrier concentration and the strengthened GBS.

The single parabolic band (SPB) model, which is applicable under the condition of the acoustic phonon dominating the carrier scattering, is used to study the S-n_H and μ_H-n_H relationship and predict the optimal n_H to achieve the highest electrical performance in this work [15,41]. At room temperature, the S-n_H relation fits well the SPB Pisarenko curves (i.e., S vs. n_H), with the density-of-states effective mass (m^*_{DOS}) of 0.78 m_e (Figure 4a), which is close to those of coarse grain-$In_{0.99}Ga_{0.01}Te$ [15], $In_{0.999}Pb_{0.001}Te$ [21], InTe ingot [16], and InTe single crystal [29]. For InTe, there are complex carrier scattering mechanisms, including GBS, APS, and point defect scattering (DPS), as well as intervalley scattering and ionized impurity scattering [15,22,25,26]. However, it seems that the mixed scattering mechanism does not affect the Seebeck coefficient trend significantly. However, the μ_H is strongly related to the scattering mechanisms; this means that μ_H will increase with the elimination of GBS, which can be illustrated by the μ_H-n_H relation, as shown in Figure 4b. Therefore, removing the GBS can significantly increase the electrical properties.
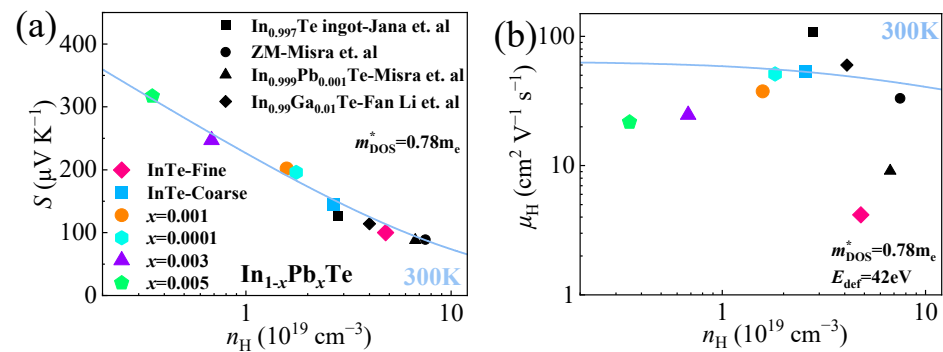
Figure 4. Room temperature Seebeck coefficient (**a**) and carrier mobility (**b**) versus the carrier concentration for the samples studied herein in comparison with the data in literature [15,16,21,29].
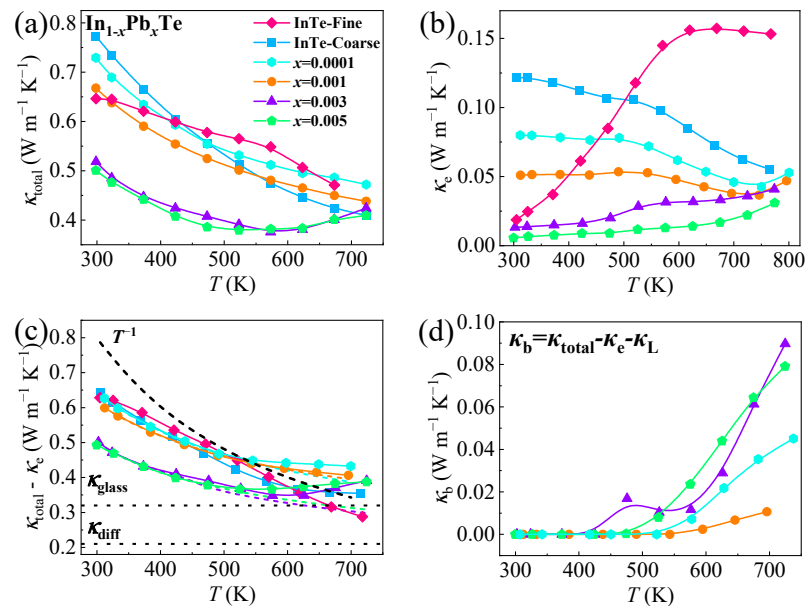
The sieved coarse $In_{1-x}Pb_xTe$ (x = 0, 0.0001, 0.001, 0.003, 0.005) with a high texture degree of the (*ll*0) plane can utilize the extraordinarily low thermal conductivity of InTe along the [110] direction. In addition, the doping of the heavy atom Pb can further introduce the point defect to reduce the lattice thermal conductivity (κ_L) and thus produce extremely low total thermal conductivity (κ_{total}), as shown in Figure 5a. At room temperature, the κ_{total} tonelessly decreased with the increase in the doping amount due to the intensified point defect derived from the fluctuations of the atomic mass and radius. In addition, the κ_{total} of all the samples normally decreased with the increase in temperature below 500 K for the increased phonon–phonon scattering as the temperature increased. However, the κ_{total} for the doped samples showed a slight upturn when the temperature was higher than 500 K, indicating the contribution of the bipolar diffusion and the recombination, which was analyzed above. In order to evaluate the intrinsic κ_L, the electron thermal conductivity (κ_e) was first calculated according to the Wiedemann–Franz law and is expressed as [42]:

$$\kappa_e = L\sigma T, L = 1.5 + \exp\left[-|S|/116\right] \tag{5}$$

where L is the Lorenz number, σ is the electrical conductivity, and T is the absolute temperature. The L can be estimated from the experimental Seebeck coefficient. Being consistent with the electrical conductivity, κ_e reduces with the increase in the doping ratio, as shown in Figure 5b. As noted in the Debye model, the dominant Umklapp scattering indicates that κ_L and T obey the relation of $\kappa_L = aT^{-1} + b$ above the Debye temperature [43,44]. Thus, the lattice thermal conductivity was first estimated by subtracting κ_e from κ_{total} within 300–400 K and then extrapolated in the subsequent temperature range, as shown in Figure 5c. It is clear that, with increased Pb doping, κ_L can be reduced by 23% at 300 K to 0.49 Wm^{-1} K^{-1} and by 16% at 700 K to 0.30 Wm^{-1} K^{-1}, which is lower than the limit of κ_{glass} ~ 0.32 Wm^{-1} K^{-1} with the Cahill model [45] and close to the limit of κ_{diff} ~ 0.21 Wm^{-1} K^{-1} with the diffusion model [46]. The traditional Cahill model is expressed as:

$$\kappa_{glass} \approx 1.21n^{2/3}k_B\frac{1}{3}(2v_t + v_l) \tag{6}$$

where n is the number density of the atoms, k_B is the Boltzmann constant, v_t is the transverse sound velocity, and v_l is the longitudinal sound velocity. In addition, the κ_b of each sample was calculated with the expression $\kappa_b = \kappa_{total} - \kappa_e - \kappa_L$, as shown in Figure 5d; this reveals the increased contribution of κ_b with the increase in the temperature and doping amount. Therefore, in order to obtain a high thermal conductivity of the thermoelectric material at high temperature, a suitably large band gap is necessary in order to avoid the powerful influence of bipolar diffusion.

Figure 5. Temperature dependence of the thermal properties of the sieved coarse $In_{1-x}Pb_xTe$ ($x = 0$, 0.0001, 0.001, 0.003, 0.005) and the sieved fine InTe. (**a**) Total thermal conductivity, (**b**) electron thermal conductivity, (**c**) lattice thermal conductivity. The solid part is calculated by κ_{total}-κ_e, and the dashed part is obtained by fitting the solid part within 300–400 K according to $aT^{-1} + b$, which is then extrapolated in the subsequent temperature range. The dotted lines are the minimum thermal conductivity calculated by Chaill model and diffusion model [45,46]. (**d**) Bipolar thermal conductivity.

The calculated zT values of all the samples, based on the measured electrical and thermal properties, are presented in Figure 6. Due to the simultaneously optimized electrical and thermal conductivity, the zT value increased from 0.02 for polycrystalline InTe with fine grains to 0.2 for the coarse one and further to 0.26 for $In_{0.9999}Pb_{0.0001}Te$ with coarse grains at room temperature. In addition, the peak zT value can also be increased from 0.54 to 0.70 with the increase in the grains. Because of the depression of GBS when $x < 0.3\%$ and the high texture degree of the (110) plane, the average zT of coarse grain-$In_{1-x}Pb_xTe$ sample can also be increased greatly; this was calculated by the following equation:

$$zT_{avg} = \frac{\int_{300}^{623} zT(T)dT}{\Delta T} \qquad (7)$$
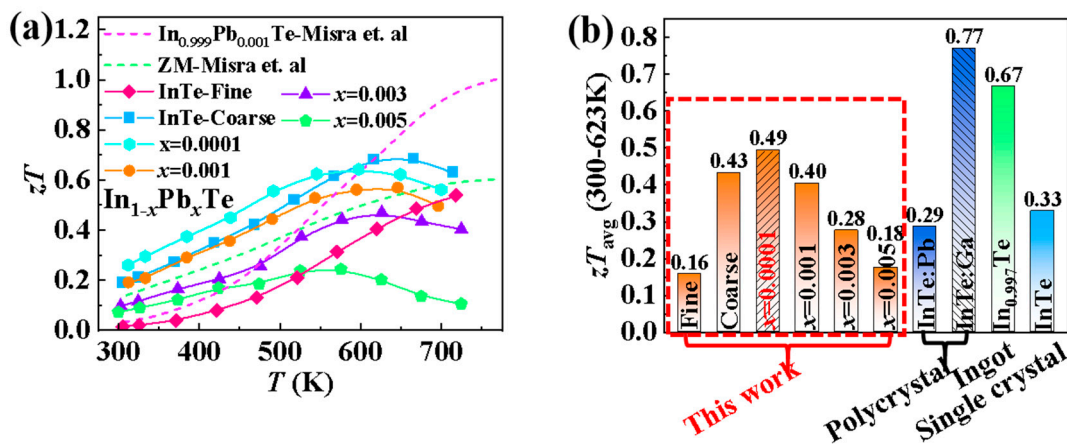
Figure 6. (**a**) Temperature dependence of zT, (**b**) the average zT within 300–623 K for our $In_{1-x}Pb_xTe$ ($x = 0$, 0.0001, 0.001, 0.003, 0.005) samples in comparison with the values in other literature [15,16,21,29].

In detail, the zT_{avg} increased by 168%, from 0.16 to 0.43, with the increasing grain size and further increased by 14% to 0.49 with Pb doping. This value is much higher than that of the Pb-doped (0.29) sample with fine grain in the literature and ranks higher among all the reported polycrystalline InTe-based TE materials, as shown in Figure 6b.

4. Conclusions

In summary, in order to fully investigate the mechanism of the grain boundary scattering of InTe, we systematically explored the synergistic effect of grain size and the carrier concentration on the carrier scattering mechanism with selective Pb doping at the In$^+$ site. This design could monotonically reduce the carrier concentration, which provided the opportunity to explore the effect of carrier concentration on the suppression of GBS for InTe. When the carrier concentration was high, the grain size dominated the GBS, and merely increasing the grain sizes could depress the GBS. However, when the carrier concentration was low ($<0.7 \times 10^{19}$ cm^{-3}) the GBS was still strong even for the coarse polycrystalline InTe. In addition, the Pb doping monotonically reduced the lattice thermal conductivity. As a result, the Pb$_{0.0001}$In$_{0.9999}$Te achieved the improved power factor and high peak zT value of 0.65@720K, as well as the average zT value of 0.49 within 300–623 K, which was beneficial to the power generation below a medium temperature. This work uncovers the influence of grain size and the carrier concentration for the grain boundary scattering of a semiconductor, which is helpful in improving the TE performance by the grain boundary scattering modulation of other materials via the synergistic effect of increasing grain size and carrier concentration.

References

1. Bell, L.E. Cooling, Heating, Generating Power, and Recovering Waste Heat with Thermoelectric Systems. *Science* **2008**, *321*, 1457–1461. [CrossRef] [PubMed]
2. Jiang, B.; Wang, W.; Liu, S.; Wang, Y.; Wang, C.; Chen, Y.; Xie, L.; Huang, M.; He, J. High figure-of-merit and power generation in high-entropy GeTe-based thermoelectrics. *Science* **2022**, *377*, 208–213. [CrossRef]
3. Nandihalli, N.; Gregory, D.H.; Mori, T. Energy-Saving Pathways for Thermoelectric Nanomaterial Synthesis: Hydrothermal/Solvothermal, Microwave-Assisted, Solution-Based, and Powder Processing. *Adv. Sci.* **2022**, *9*, 2106052. [CrossRef] [PubMed]
4. Snyder, G.J.; Toberer, E.S. Complex thermoelectric materials. *Nat. Mater.* **2008**, *7*, 105–114. [CrossRef] [PubMed]
5. Heremans, J.P.; Jovovic, V.; Toberer, E.S.; Saramat, A.; Kurosaki, K.; Charoenphakdee, A.; Yamanaka, S.; Snyder, G.J. Enhancement of Thermoelectric Efficiency in PbTe by Distortion of the Electronic Density of States. *Science* **2008**, *321*, 554–557. [CrossRef]
6. Ahmad, M.; Agarwal, K.; Munoz, S.G.; Ghosh, A.; Kodan, N.; Kolosov, O.V.; Mehta, B.R. Engineering Interfacial Effects in Electron and Phonon Transport of Sb$_2$Te$_3$/MoS$_2$ Multilayer for Thermoelectric ZT Above 2.0. *Adv. Funct. Mater.* **2022**, *32*, 2206384. [CrossRef]
7. Pei, Y.; LaLonde, A.D.; Wang, H.; Snyder, G.J. Low effective mass leading to high thermoelectric performance. *Energy Environ. Sci.* **2012**, *5*, 7963–7969. [CrossRef]

8. Yan, X.; Poudel, B.; Ma, Y.; Liu, W.S.; Joshi, G.; Wang, H.; Lan, Y.; Wang, D.; Chen, G.; Ren, Z.F. Experimental studies on anisotropic thermoelectric properties and structures of n-type $Bi_2Te_{2.7}Se_{0.3}$. *Nano Lett.* **2010**, *10*, 3373–3378. [CrossRef]

9. Nunna, R.; Qiu, P.; Yin, M.; Chen, H.; Hanus, R.; Song, Q.; Zhang, T.; Chou, M.Y.; Agne, M.T.; He, J.; et al. Ultrahigh thermoelectric performance in Cu_2Se-based hybrid materials with highly dispersed molecular CNTs. *Energy Environ. Sci.* **2017**, *10*, 1928–1935. [CrossRef]

10. Zhao, L.; Tan, G.; Hao, S.; He, J.; Pei, Y.; Chi, H.; Wang, H.; Gong, S.; Xu, H.; Dravid, V.P.; et al. Ultrahigh power factor and thermoelectric performance in holedoped single-crystal SnSe. *Science* **2015**, *351*, 141–144. [CrossRef] [PubMed]

11. Wang, D.; Liu, W.; Li, M.; Yin, L.; Gao, H.; Sun, Q.; Wu, H.; Wang, Y.; Shi, X.; Yang, X.; et al. Simultaneously achieving high ZT and mechanical hardness in highly alloyed GeTe with symmetric nanodomains. *Chem. Eng. J.* **2022**, *441*, 136131. [CrossRef]

12. Mao, J.; Wu, Y.; Song, S.; Zhu, Q.; Shuai, J.; Liu, Z.; Pei, Y.; Ren, Z. Defect Engineering for Realizing High Thermoelectric Performance in n-Type Mg_3Sb_2-Based Materials. *ACS Energy Lett.* **2017**, *2*, 2245–2250. [CrossRef]

13. Ma, J.; Delaire, O.; May, A.F.; Carlton, C.E.; McGuire, M.A.; VanBebber, L.H.; Abernathy, D.L.; Ehlers, T.H.G.; Huq, A.; Tian, W.; et al. Glass-like phonon scattering from a spontaneous nanostructure in $AgSbTe_2$. *Nat. Nanotechnol.* **2013**, *8*, 445–451. [CrossRef] [PubMed]

14. Detemple, R.; Wamwangi, D.; Wuttig, M.; Bihlmayer, G. Identification of Te alloys with suitable phase change characteristics. *Appl. Phys. Lett.* **2003**, *83*, 2572–2574. [CrossRef]

15. Li, F.; Liu, X.; Ma, N.; Chen, L.; Wu, L.M. Thermoelectric Zintl Compound $In_{1−x}Ga_xTe$: Pure Acoustic Phonon Scattering and Dopant-Induced Deformation Potential Reduction and Lattice Shrink. *Angew. Chem. Int. Ed.* **2022**, *61*, e202208216.

16. Jana, M.K.; Pal, K.; Waghmare, U.V.; Biswas, K. The Origin of Ultralow Thermal Conductivity in InTe: Lone-Pair-Induced Anharmonic Rattling. *Angew. Chem. Int. Ed.* **2016**, *55*, 7923–7927. [CrossRef]

17. Wang, D.; Liu, W.; Li, M.; Zheng, K.; Hu, H.; Yin, L.; Wang, Y.; Zhu, H.; Shi, X.L.; Yang, X.; et al. Hierarchical Architectural Structures Induce High Performance in n-Type GeTe-Based Thermoelectrics. *Adv. Funct. Mater.* **2023**, 2213040. [CrossRef]

18. Slack, G.A.; Rowe, D.M. *CRC Handbook of Thermoelectrics*; CRC Press: Boca Raton, FL, USA, 1995.

19. Nolas, G.; Morelli, D.; Tritt, T.M. Skutterudites: A Phonon-Glass-Electron Crystal Approach to Advanced Thermoelectric Energy Conversion Applications. *Annu. Rev. Mater. Sci.* **1999**, *29*, 89–116. [CrossRef]

20. Parlak, M.; Ercelebi, C.; Gunal, I.; Ozkan, H.; Gasanly, N.M. Anisotropy of Electrical Resistivity and Hole Mobility in InTe Single Crystals. *Cryst. Res. Technol.* **1996**, *31*, 673–678. [CrossRef]

21. Misra, S.; Léon, A.; Levinský, P.; Hejtmánek, J.; Lenoir, B.; Candolfi, C. Enhanced thermoelectric performance of InTe through Pb doping. *J. Mater. Chem. C* **2021**, *9*, 14490–14496. [CrossRef]

22. Zhu, H.; Zhang, B.; Wang, G.; Peng, K.; Yan, Y.; Zhang, Q.; Han, X.; Wang, G.; Lu, X.; Zhou, X. Promoted high temperature carrier mobility and thermoelectric performance of InTe enabled by altering scattering mechanism. *J. Mater. Chem. A* **2019**, *7*, 11690–11698. [CrossRef]

23. Pan, S.; Liu, H.; Li, Z.; You, L.; Dai, S.; Yang, J.; Guo, K.; Luo, J. Enhancement of the thermoelectric performance of InTe via introducing Cd dopant and regulating the annealing time. *J. Alloys Compd.* **2020**, *813*, 152210–152216. [CrossRef]

24. Huang, R.; Huang, Y.; Zhu, B.; He, M.; Ge, Z.; Fu, L.; He, J. Large enhancement of thermoelectric performance of InTe compound by sintering and $CuInTe_2$ doping. *J. Appl. Phys.* **2019**, *126*, 125108. [CrossRef]

25. Back, S.Y.; Kim, Y.K.; Cho, H.; Han, M.K.; Kim, S.J.; Rhyee, J.S. Temperature-Induced Lifshitz Transition and Charge Density Wave in $InTe_{1−δ}$ Thermoelectric Materials. *ACS Appl. Energy Mater.* **2020**, *3*, 3628–3636. [CrossRef]

26. Back, S.Y.; Cho, H.; Kim, Y.K.; Byeon, S.; Jin, H.; Koumoto, K.; Rhyee, J.S. Enhancement of thermoelectric properties by lattice softening and energy band gap control in Te-deficient $InTe_{1−δ}$. *AIP Adv.* **2018**, *8*, 115227–115237. [CrossRef]

27. Zhu, H.; Wang, G.; Wang, G.; Zhou, X.; Lu, X. The role of electronic affinity for dopants in thermoelectric transport properties of InTe. *J. Alloys Compd.* **2021**, *869*, 159224–159229. [CrossRef]

28. Lotgering, F.K. Topotactical Reactions With Ferrimagnetic Oxides Having Hexagonal Crystal Structures—I. *J. Inorg. Nucl. Chem* **1959**, *9*, 113–123. [CrossRef]

29. Misra, S.; Levinský, P.; Dauscher, A.; Medjahdi, G.; Hejtmánek, J.; Malaman, B.; Snyder, G.J.; Lenoir, B.; Candolfi, C. Synthesis and physical properties of single-crystalline InTe: Towards high thermoelectric performance. *J. Mater. Chem. C* **2021**, *9*, 5250–5260. [CrossRef]

30. Wu, Y.; Liu, F.; Zhang, Q.; Zhu, T.; Xia, K.; Zhao, X. Enhancing the average thermoelectric figure of merit of elemental Te by suppressing grain boundary scattering. *J. Mater. Chem. A* **2020**, *8*, 8455–8461. [CrossRef]

31. Qiu, Q.; Liu, Y.; Xia, K.; Fang, T.; Yu, J.; Zhao, X.; Zhu, T. Grain Boundary Scattering of Charge Transport in n-Type (Hf, Zr)CoSb Half-Heusler Thermoelectric Materials. *Adv. Energy Mater.* **2019**, *9*, 1803447. [CrossRef]

32. Hogg, J.H.C.; Sutherland, H.H. Indium Telluride. *Acta Cryst.* **1976**, *32*, 2689–2690. [CrossRef]

33. Nandihalli, N.; Pai, Y.H.; Liu, C.J. Fabrication and thermoelectric properties of $Pb_{1-y}(Zn_{0.85}Al_{0.15})_yTe$-Te (*y* = 0, 0.04, 0.06, 0.08, and 0.11) nanocomposites. *Ceram. Int.* **2020**, *46*, 6443–6453. [CrossRef]

34. Kamins, T.I. Hall Mobility in Chemically Deposited Polycrystalline Silicon. *J. Appl. Phys.* **1971**, *42*, 4357–4365. [CrossRef]

35. Seto, J.Y.W. The electrical properties of polycrystalline silicon films. *J. Appl. Phys.* **1975**, *46*, 5247–5254. [CrossRef]

36. Hu, C.; Xia, K.; Fu, C.; Zhao, X.; Zhu, T. Carrier grain boundary scattering in thermoelectric materials. *Energy Environ. Sci.* **2022**, *15*, 1406–1422. [CrossRef]

37. He, R.; Kraemer, D.; Mao, J.; Zeng, L.; Jie, Q.; Lan, Y.; Li, C.; Shuai, J.; Kim, H.S.; Liu, Y.; et al. Achieving high power factor and output power density in p-type half-Heuslers $Nb_{1-x}Ti_xFeSb$. *Proc. Natl. Acad. Sci. USA* **2016**, *113*, 13576–13581. [CrossRef]

38. Fu, C.; Wu, H.; Liu, Y.; He, J.; Zhao, X.; Zhu, T. Enhancing the Figure of Merit of Heavy-Band Thermoelectric Materials Through Hierarchical Phonon Scattering. *Adv. Sci.* **2016**, *3*, 1600035. [CrossRef] [PubMed]

39. Wood, M.; Kuo, J.J.; Imasato, K.; Snyder, G.J. Improvement of Low-Temperature zT in a Mg_3Sb_2-Mg_3Bi_2 Solid Solution via Mg-Vapor Annealing. *Adv. Mater.* **2019**, *31*, 1902337. [CrossRef]

40. Goldsmid, H.J.; Sharp, J.W. Estimation of the thermal band gap of a semiconductor from seebeck measurements. *J. Electron. Mater.* **1999**, *28*, 869–872. [CrossRef]

41. Zhu, J.; Zhang, X.; Guo, M.; Li, J.; Hu, J.; Cai, S.; Cai, W.; Zhang, Y.; Sui, J. Restructured single parabolic band model for quick analysis in thermoelectricity. *npj Comput. Mater.* **2021**, *7*, 116. [CrossRef]

42. Graf, M.J.; Yip, S.K.; Sauls, J.A. Electronic thermal conductivity and the Wiedemann-Franz law for unconventional superconductors. *Phys. Rev. B* **1996**, *53*, 15147–15160. [CrossRef] [PubMed]

43. Hao, F.; Xing, T.; Qiu, P.; Hu, P.; Wei, T.; Ren, D.; Shi, X.; Chen, L. Enhanced Thermoelectric Performance in n-Type Bi_2Te_3-Based Alloys via Suppressing Intrinsic Excitation. *ACS Appl. Mater. Interfaces* **2018**, *10*, 21372–21380. [CrossRef] [PubMed]

44. Blank, V.D.; Buga, S.G.; Kulbachinskii, V.A.; Kytin, V.G.; Medvedev, V.V.; Popov, M.Y.; Stepanov, P.B.; Skok, V.F. Thermoelectric properties of $Bi_{0.5}Sb_{1.5}Te_3/C_{60}$ nanocomposites. *Phys. Rev. B* **2012**, *86*, 075426. [CrossRef]

45. Cahill, D.G.; Watson, S.K.; Pohl, R.O. Lower limit to the thermal conductivity of disordered crystals. *Phys. Rev. B* **1992**, *46*, 6131–6140. [CrossRef]

46. Agne, M.T.; Hanus, R.; Snyder, G.J. Minimum thermal conductivity in the context of diffuson-mediated thermal transport. *Energy Environ. Sci.* **2018**, *11*, 609–616. [CrossRef]